



Enhancement of the lattice thermal conductivity of two-dimensional functionalized MXenes by inversion symmetry breaking

Shuang Lu, Weijun Ren, Jia He, Cuiqian Yu , Pengfei Jiang, and Jie Chen ^{*}

Center for Phononics and Thermal Energy Science, China-EU Joint Lab for Nanophononics, MOE Key Laboratory of Advanced Micro-structured Materials, School of Physics Science and Engineering, Tongji University, Shanghai 200092, People's Republic of China



(Received 6 January 2022; accepted 22 March 2022; published 4 April 2022)

Crystal symmetry plays a critical role in thermal transport in solids. One example is mirror symmetry in monolayer graphene that promotes thermal transport by forbidding certain phonon scattering channels. Here, we show an interesting counterexample in monolayer Ta_2CS_2 that inversion symmetry breaking can abnormally enhance lattice thermal conductivity of two-dimensional (2D) functionalized MXenes based on the phonon Boltzmann transport theory combined with first-principles calculations. We find inversion symmetry breaking not only affects scattering channels but also redistributes the charge and changes the anharmonic phonon properties. Both atomic vibrations in real space and phonon scattering rates in the reciprocal space confirm the significantly reduced lattice anharmonicity in an asymmetric Ta_2CS_2 sheet, leading to substantially enhanced thermal conductivity after inversion symmetry breaking. The physical origin for the variation of anharmonic properties induced by symmetry is discussed in detail. In this paper, we provide insight into the complex role of symmetry on thermal transport in 2D functionalized MXenes.

DOI: [10.1103/PhysRevB.105.165301](https://doi.org/10.1103/PhysRevB.105.165301)

I. INTRODUCTION

In the past several decades, thermoelectric devices have attracted great attention because of their high potential in many areas including power generators, cooling devices, and sensors [1–5]. Thermoelectric materials can directly convert thermal energy into electrical energy and vice versa through the flow of charge carriers in solid state [6–8]. The thermoelectric performance of the material is evaluated by the dimensionless figure of merit $ZT = \sigma S^2 T / \kappa$, where σ , S , κ , and T correspond to the electrical conductivity, the Seebeck coefficient, thermal conductivity, and the absolute temperature, respectively. ZT can thus be enhanced by increasing the power factor ($S^2\sigma$) and/or by reducing the thermal conductivity, but the complex interdependency of power factor and thermal conductivity makes it challenging to enhance the ZT value [9].

Recent experimental and theoretical results confirm that reduction of thermal conductivity can be achieved by several mechanisms. Nanostructuring, such as embedded nanoparticles, boundaries, and superlattices, can effectively reduce thermal conductivity by enhancing the phonon scattering rates [10–15]. Resonant scatterings such as cage structures and pillared nanostructures can also significantly reduce the thermal conductivity by increasing the number of scattering channels [16–20]. Increasing the complexity of the crystal or forming alloy is also effective for the reduction of thermal conductivity by breaking mode degeneracy and thus increasing the phonon scattering channels [21–24]. The abovementioned methods require either disrupting the periodicity of the crystal or

changing the lattice structure or the types of atoms. However, disrupting the lattice periodicity can also jeopardize the stability of the system, and the synthesis of stable complex crystals is also difficult in the experiment. Therefore, it is highly desirable to achieve tunable thermal conductivity of simple crystals without disrupting the lattice structure.

Authors of previous studies have shown that the symmetry and the functional atom sites in crystals have a strong impact on the electrical [25,26], magnetic [27,28], and optical properties [29,30]. Additionally, the selection rule of phonon scattering in two-dimensional (2D) materials such as graphene [31] depends strongly on the mirror symmetry. More importantly, the atom sites can also affect the charge distribution of atoms and the interaction between different phonon modes [32,33]. The effects of symmetry and atom sites are mainly on the higher-order phonon scatterings, which allows for the regulation of thermal conductivity via anharmonic interactions.

Ferroelectric materials are systems with spontaneous symmetry breaking, which is characterized by the ordered electric polarization. Due to the impact of symmetry on thermal conductivity, the response of ferroelectric materials to external electric fields makes it possible to dynamically control the thermal transport. Transition metal carbides, carbonitrides, and nitrides (MXenes) have a general formula [34] of $M_{n+1}X_n$ ($n = 1-3$), where M represents a transition metal element (such as Sc, Ti, Hf, Nb, Ta, or Mo, among others), and X is carbon and/or nitrogen. The ferroelectricity in MXenes has been realized by surface functionalization. A variety of functional groups, such as O, OH, F, Cl, and S, can be utilized in experiment to functionalize the surface of MXenes [35–37]. Some MXene structures exhibit semiconducting behavior with a small bandgap [37,38], such as Nb_2CS_2 and Ta_2CS_2 . This suggests that these functionalized MXenes

^{*}Corresponding author: jie@tongji.edu.cn

would be good candidates for thermoelectric applications. Furthermore, unlike most ferroelectric materials, the highly symmetrically functionalized MXenes also have a minimum potential energy. Additionally, the energy difference between the high- and low-symmetry phases is small, which indicates a first-order nonpolar-polar structural phase transition and the possible coexistence of the high- and low-symmetry phases. This provides a promising platform to study the influence of symmetry and atom sites [38,39].

In this paper, we study the lattice thermal conductivity of the ferroelectric material Ta₂CS₂ with both symmetric and asymmetric phases based on the Peierls-Boltzmann transport equation. It is found that thermal conductivity of asymmetric Ta₂CS₂ is much higher than that of symmetric Ta₂CS₂, which is in sharp contrast to the role of symmetry in typical 2D materials such as graphene. The detailed analysis reveals that the lower stability and stronger coupling between phonon branches in symmetric Ta₂CS₂ lead to the stronger anharmonic scattering strength, leading to a lower thermal conductivity.

The rest of the paper is organized as follows. The computational methodology is described in Sec. II. In Sec. III, we present the thermal conductivity results of symmetric Ta₂CS₂ and asymmetric Ta₂CS₂. The anharmonic properties are systematically investigated to explore the origin for the observed difference in thermal conductivity. The conclusions are summarized in Sec. IV.

II. COMPUTATIONAL METHODS

The first-principles calculations based on density functional theory were carried out with the Vienna *Ab initio* Simulation Package (VASP) [40,41]. The exchange-correlation of valence electrons was described by generalized gradient approximation of the Perdew-Burke-Ernzerhof type [42]. The cutoff energy for plane waves was set to 600 eV, and the first Brillouin zone of all structures was sampled with a $15 \times 15 \times 1$ k-point grid centered on the Γ point [43]. A large vacuum layer of 15 Å was included to separate the interaction in the vertical direction. The dipole correction along the vertical direction was also applied in our calculation since there exists a net dipole in the ferroelectric system [44]. The structures were completely relaxed until the maximum force acting on the atoms and the energy of the entire system converged to 1×10^{-4} eV Å⁻¹ and 1×10^{-7} eV, respectively. The *ab initio* molecular dynamics (AIMD) simulations were performed for 10 ps in the canonical (NVT) ensemble with a time step of 1 fs, and the Nosé-Hoover method was applied to control the temperature.

The harmonic (2ND) and the third-order (3RD) anharmonic interatomic force constants (IFCs) were computed by the finite displacement method as implemented in the PHONOPY code [45] and the SHENGBTE code [46], respectively. A $4 \times 4 \times 1$ supercell with a $3 \times 3 \times 1$ k-mesh for sampling is used to obtain the harmonic and anharmonic IFCs. More details can be found in our previous works [47–49].

In the linearized phonon Boltzmann transport equation (BTE), the lattice thermal conductivity is calculated as

$$\kappa_L^{\alpha\beta} = \frac{1}{k_B T^2 N V} \sum_{\lambda} f_{\lambda}^0 (f_{\lambda}^0 + 1) (\hbar \omega_{\lambda})^2 v_{\lambda}^{\alpha} F_{\lambda}^{\beta}, \quad (1)$$

where k_B , T , \hbar , V , and N are the Boltzmann constant, absolute temperature, reduced Planck's constant, the volume of the unit cell, and the total number of \mathbf{q} points uniformly spaced in the Brillouin zone, respectively. Here, ω_{λ} denotes the phonon frequency of wave vector \mathbf{q} with a branch index λ . Here, v_{λ}^{α} represents the component of the group velocity along the α direction, and f_{λ}^0 is the Bose-Einstein distribution function for the phonon population. Here, F_{λ}^{β} can be expressed as

$$F_{\lambda}^{\beta} = \tau_{\lambda}^0 (v_{\lambda}^{\beta} + \Delta_{\lambda}^{\beta}), \quad (2)$$

where τ_{λ}^0 is the phonon lifetime of phonon mode λ as obtained from perturbation theory, and Δ_{λ}^{β} is a correction term obtained by the fully iterative solution of the BTE. The total scattering rate is the sum of the isotope scattering rate and the anharmonic scattering rate $\frac{1}{\tau_{\lambda}^0} = \frac{1}{\tau_{\text{3ph},\lambda}^0} + \frac{1}{\tau_{\text{iso},\lambda}^0}$. The anharmonic three-phonon scattering process is the dominating scattering mechanism in pristine crystals, and the resulting phonon lifetime can be calculated based on the Fermi golden rule as

$$\tau_{\text{3ph},\lambda}^0 = N \left(\sum_{\lambda_1 \lambda_2} \Gamma_{\lambda \lambda_1 \lambda_2}^+ + \frac{1}{2} \sum_{\lambda_1 \lambda_2} \Gamma_{\lambda \lambda_1 \lambda_2}^- \right)^{-1}, \quad (3)$$

where $\Gamma_{\lambda \lambda_1 \lambda_2}^+$ and $\Gamma_{\lambda \lambda_1 \lambda_2}^-$ represent the scattering rates for the absorbing and emitting three-phonon scattering processes, respectively. The phonon scattering rates are given by

$$\begin{aligned} \Gamma_{\lambda \lambda_1 \lambda_2}^+ &= \frac{\hbar \pi}{4} \frac{(f_{\lambda}^0 - f_{\lambda_1}^0 - f_{\lambda_2}^0)}{\omega_{\lambda} \omega_{\lambda_1} \omega_{\lambda_2}} |V_{\lambda \lambda_1 \lambda_2}^+|^2 \delta(\omega_{\lambda} + \omega_{\lambda_1} - \omega_{\lambda_2}), \\ \Gamma_{\lambda \lambda_1 \lambda_2}^- &= \frac{\hbar \pi}{4} \frac{(f_{\lambda}^0 + f_{\lambda_1}^0 + f_{\lambda_2}^0)}{\omega_{\lambda} \omega_{\lambda_1} \omega_{\lambda_2}} |V_{\lambda \lambda_1 \lambda_2}^-|^2 \delta(\omega_{\lambda} - \omega_{\lambda_1} - \omega_{\lambda_2}). \end{aligned} \quad (4)$$

The $V_{\lambda \lambda_1 \lambda_2}^{\pm}$ are the scattering matrix elements given by [50]

$$V_{\lambda \lambda_1 \lambda_2}^{\pm} = \sum_{i,j,k} \sum_{\alpha\beta\gamma} \Phi_{ijk}^{\alpha\beta\gamma} \frac{e_{\pm\lambda}^{i\alpha} e_{\pm\lambda_1}^{j\beta} e_{\pm\lambda_2}^{k\gamma}}{\sqrt{m_i m_j m_k}}, \quad (6)$$

where $\Phi_{ijk}^{\alpha\beta\gamma}$ is the 3RD anharmonic IFCs, i , j , and k are the atomic indices; m is the atomic mass; and $e_{\lambda}^{i\alpha}$ is the α th component of the phonon eigenvector on the atom. A cutoff distance up to the seventh nearest neighbor is used to ensure the convergence of thermal conductivity. The stopping criterion for the iteration process is that the relative change in the calculated thermal conductivity tensor is $< 10^{-5}$.

III. RESULTS AND DISCUSSION

The primitive cells of the asymmetric and symmetric Ta₂CS₂ sheets are shown in Fig. 1. For asymmetric Ta₂CS₂, one S atom is above the Ta atom, while another S atom is above the C atom, causing inversion symmetry breaking. After structure optimization, the lattice constant of symmetric Ta₂CS₂ monolayer is $a = b = 3.260$ Å, and it is $a = b = 3.242$ Å in asymmetric Ta₂CS₂. The space group of symmetric Ta₂CS₂ is *P*-3m1 (164), while that of asymmetric Ta₂CS₂ is *P*3m1 (156). Due to the lack of inversion symmetry, there are different bond types of Ta-S and Ta-C in asymmetric Ta₂CS₂

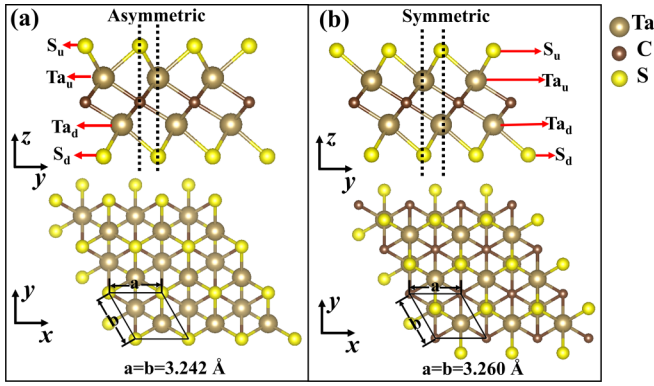


FIG. 1. (a) The side and top views of asymmetric Ta_2CS_2 and (b) symmetric Ta_2CS_2 . The black dotted line represents the position of the S atom. In asymmetric Ta_2CS_2 , one S atom is located above the C atom, and another is above the Ta atom (dot lines). All S atoms are located above the Ta atom for symmetric Ta_2CS_2 .

[see Fig. 1(a)]. Although the corresponding bond lengths of asymmetric Ta_2CS_2 are almost the same as that of symmetric Ta_2CS_2 , the stabilities and vibrational and thermal properties have significant differences due to symmetry breaking and the existence of the net dipole.

The polarization switching process via the displacement of the S atom is calculated by the nudged elastic band (NEB) method [51], as shown in Fig. 2(a). Asymmetric Ta_2CS_2 has slightly lower energy than symmetric Ta_2CS_2 , which means asymmetric Ta_2CS_2 is more stable. The potential barrier between symmetric and asymmetric Ta_2CS_2 is 1.28 eV, and the deep potential well results in the coexistence of symmetric Ta_2CS_2 and asymmetric Ta_2CS_2 , which is different from the common ferroelectric materials.

To further verify the stability, the phonon dispersions along the high-symmetry path of these two monolayers are calculated. Long-range electrostatic interactions (nonanalyt-

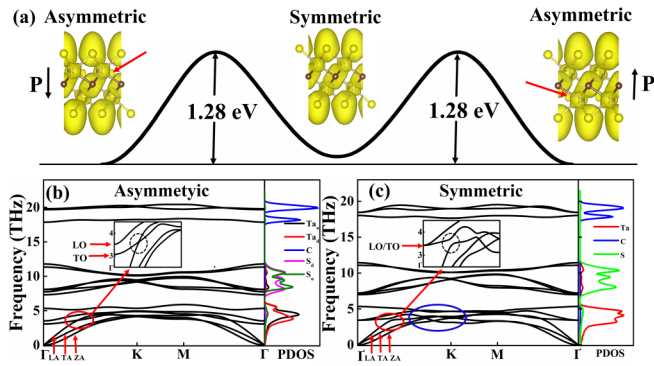


FIG. 2. (a) Nudged elastic band (NEB) calculations of asymmetric Ta_2CS_2 and symmetric Ta_2CS_2 . The electron localization function (ELF) is also shown. The high charge localization region appears between Ta and S atoms in asymmetric Ta_2CS_2 as indicated by the red arrows, and the P on both sides represents the direction of polarization. (b) Phonon dispersion and phonon density of states (PDOS) of asymmetric Ta_2CS_2 and (c) symmetric Ta_2CS_2 . The inset images show longitudinal acoustic (LA)-transverse optical (TO) hybridization of asymmetric and symmetric Ta_2CS_2 .

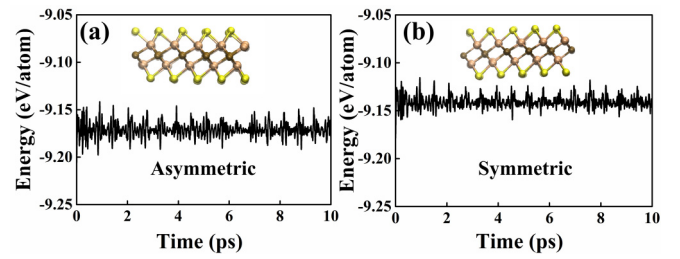


FIG. 3. (a) The evolution of the average energy per atom of the *ab initio* molecular dynamics (AIMD) at 800 K for asymmetric Ta_2CS_2 and (b) symmetric Ta_2CS_2 .

ical correction) are included by using the Born effective charges and the dielectric tensor calculated by VASP, and the phonon frequencies at various \mathbf{q} -points are calculated using the method in Ref. [52]. As shown in Figs. 2(b) and 2(c), there is no negative frequency in the phonon dispersion for both structures, which is consistent with the literature result [38] and confirms the thermodynamic stability of the structures.

In symmetric Ta_2CS_2 , the longitudinal optical (LO) and transverse optical (TO) modes are degenerate at the Γ point [Fig. 2(c)], indicating the absence of the net dipole and long-range Coulomb interactions. In contrast, there is a splitting between the LO and TO modes at the Γ point in asymmetric Ta_2CS_2 [Fig. 2(b)] due to the presence of dipole-dipole interactions in ferroelectrics, which is related to the charge localization between the Ta-S atoms on one side of the asymmetric Ta_2CS_2 as indicated by the red arrow in Fig. 2(a). In both structures, the in-plane longitudinal acoustic (LA) mode and the transverse acoustic (TA) mode exhibit a linear dispersion around the Γ point, whereas the out-of-plane acoustic (flexural acoustic, or ZA) mode has a quadratic dispersion in the long wavelength limit, which is the characteristic of monolayer material.

Compared with asymmetric Ta_2CS_2 , the TO branch away from the Γ point in symmetric Ta_2CS_2 is softened, especially at the K point [see the blue circle region in Fig. 2(c)]. The TO branch is highly related to the phase transition in ferroelectric materials, which will be discussed later in detail. In addition, the phonon density of states (PDOS) of two structures are also shown in the right panel of Figs. 2(b) and 2(c). In both structures, the optical branches in the high-frequency region are mainly contributed by carbon atoms, the optical branches in the intermediate-frequency region are mainly contributed by sulfur atoms, and the optical or acoustic branches in the low-frequency region are mainly contributed by Ta atoms. Due to the large atomic mass difference and weak interaction, the PDOS spectrum for different kinds of atoms shows almost no overlap. The decoupling of atomic vibrations and the unequal contribution of phonons to thermal transport at different frequencies provide avenues to regulate the thermal conductivity by adjusting the harmonic/anharmonic phonon properties. Moreover, we have also performed AIMD simulations for both structures and verified that both structures are thermally stable even at 800 K, as shown in Fig. 3.

After confirming the stability of these two structures, the lattice thermal conductivity of two monolayer structures is calculated by using the iterative solution of BTE. By testing

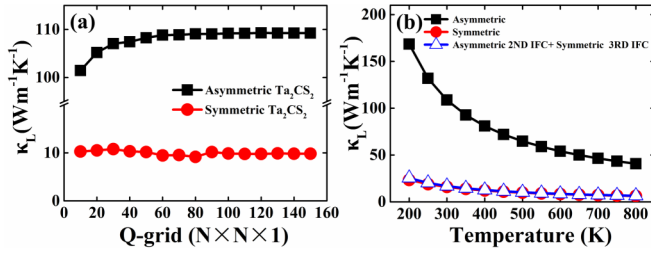


FIG. 4. (a) The convergence test of the thermal conductivity for asymmetric Ta₂CS₂ and symmetric Ta₂CS₂ at 300 K. (b) Thermal conductivity of asymmetric Ta₂CS₂ (solid square) and symmetric Ta₂CS₂ (solid circle). A hypothetical case (empty triangle) using the harmonic (2ND) interatomic force constants (IFCs) of asymmetric Ta₂CS₂, and the anharmonic (3RD) IFCs of symmetric Ta₂CS₂ are also shown for comparison.

the convergence of the thermal conductivity with respect to the Q-grid, as shown in Fig. 4(a), a dense Q-grid size of $120 \times 120 \times 1$ is used for the rest of this paper. Moreover, our calculation results further reveal that both structures are isotropic and have the same thermal conductivity in two in-plane directions.

Surprisingly, our simulation results reveal the thermal conductivity of symmetric Ta₂CS₂ is significantly lower than that of asymmetric Ta₂CS₂ at various temperatures, as shown in Fig. 4(b). For instance, the thermal conductivity of asymmetric Ta₂CS₂ is $\sim 168 \text{ Wm}^{-1} \text{ K}^{-1}$ at 200 K, while it is only $23 \text{ Wm}^{-1} \text{ K}^{-1}$ in symmetric Ta₂CS₂ at the same temperature, showing more than sevenfold enhancement after inversion symmetry breaking. This result is not consistent with previous findings on symmetry [31,53,54]. In general, the thermal conductivity of 2D materials with a high-symmetry phase is usually higher than that of the low-symmetry phase. This is because the high-symmetry phase will cause the band degeneracy and forbid certain phonon scattering channels. Such symmetry breaking will remove the constraints to the phonon scattering process, opening some scattering channels and thus suppressing the thermal transport, such as the skew graphene [54] and Janus asymmetry structures [55].

Due to the quite similar phonon dispersion between asymmetric and symmetric Ta₂CS₂ sheets (Fig. 2), we have verified in our calculations that there is no substantial difference between these two structures in the harmonic properties, such as the phonon group velocity and the phase space for three-phonon scatterings. Therefore, we speculate the change of symmetry and atom sites mainly results in the variation of anharmonic phonon scattering strength and then affects the thermal conductivity. To test our conjecture, we construct a hypothetical case in which we only replace the 3RD IFCs of asymmetric Ta₂CS₂ with the counterpart of symmetric Ta₂CS₂ and repeat the thermal conductivity calculation. As shown in Fig. 4(b), the thermal conductivity of this hypothetical case (empty triangle) is almost identical to the thermal conductivity of symmetric Ta₂CS₂ (solid circle), indicating that the anharmonic properties play a dominant role in determining the thermal conductivity of Ta₂CS₂.

The degree of anharmonicity can be directly manifested by the magnitude of atomic deviation from the equilibrium

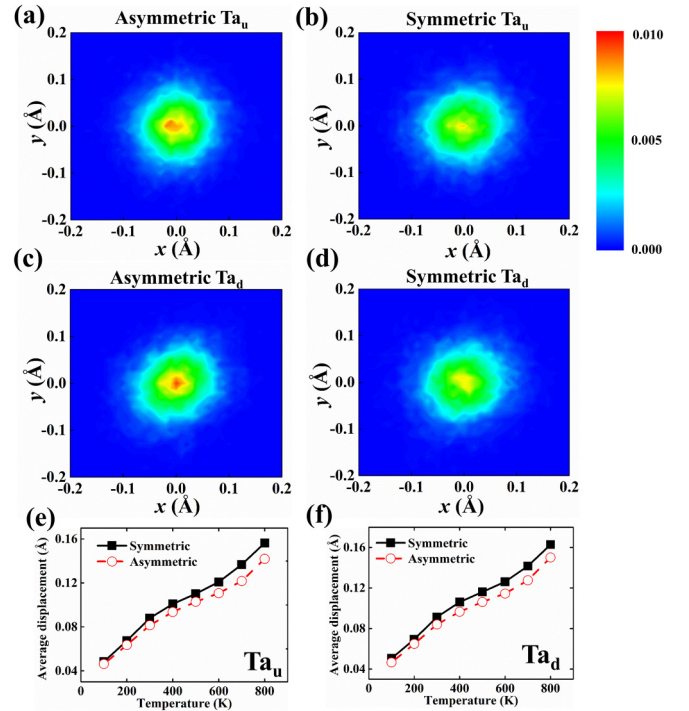


FIG. 5. Probability distributions of the Ta_u/Ta_d atom of (a) and (c) asymmetric Ta₂CS₂ and (b) and (d) symmetric Ta₂CS₂ at 300 K. Compared with symmetric Ta₂CS₂, Ta atoms in asymmetric Ta₂CS₂ are more likely to appear near the equilibrium position, indicating a weaker anharmonic effect in asymmetric Ta₂CS₂. Comparison of ensemble averaged displacement between asymmetric and symmetric Ta₂CS₂ for (e) the Ta_u atom and (f) the Ta_d atom.

position in real space at finite temperatures. Since the thermal conductivity of Ta₂CS₂ is mainly contributed by the acoustic branches in low frequencies that originate from Ta atoms (see PDOS in Fig. 2), we focus here on the probability distribution of Ta atoms in the x - y plane at 300 K, with the origin of the x - y plane denoting the equilibrium position. As shown in Fig. 5, the probability of Ta atoms in asymmetric Ta₂CS₂ appearing near the equilibrium position is significantly higher than that of symmetric Ta₂CS₂. Moreover, the ensemble averaged displacement of Ta atoms in asymmetric Ta₂CS₂ is smaller than that of symmetric Ta₂CS₂, and the difference becomes larger with increasing temperature, as shown in Figs. 5(e) and 5(f). The enlarged displacement of Ta atoms in symmetric Ta₂CS₂ intuitively confirms that symmetric Ta₂CS₂ has a stronger anharmonicity.

To further quantitatively compare the difference in anharmonicity between symmetric and asymmetric Ta₂CS₂ sheets, we calculate the anharmonic phonon scattering rates of acoustic branches in the reciprocal space. As shown in Fig. 6, we find that the anharmonic phonon scattering rates in symmetric Ta₂CS₂ (filled symbols) are more than one order of magnitude higher than that in asymmetric Ta₂CS₂ (empty symbols), especially for low-frequency phonons. Therefore, both the lattice vibration in the real space and the phonon properties in the reciprocal space confirm that symmetric Ta₂CS₂ has a stronger lattice anharmonicity than asymmetric Ta₂CS₂,

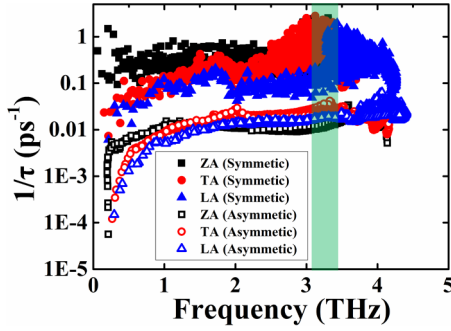


FIG. 6. Anharmonic scattering rates in symmetric Ta_2CS_2 (filled symbols) and asymmetric Ta_2CS_2 (empty symbols). The strong XY-Z hybridization causes a large anharmonic scattering rate in the shadowed region.

which causes a stronger phonon scattering and thus a lower thermal conductivity in symmetric Ta_2CS_2 .

Exploring the variation of the charge distribution and the origin of the dipole moment will be helpful for the understanding of anharmonic properties in Ta_2CS_2 . The inversion symmetry breaking makes the Ta/S atoms in asymmetric Ta_2CS_2 no longer equivalent. This inversion symmetry breaking will change the charge distribution in Ta/S atoms, resulting in the variation of anharmonic properties. In this regard, we have calculated the Bader charge following Refs. [56,57] for Ta and S atoms both in symmetric and asymmetric Ta_2CS_2 . As listed in Table I, the Bader charge of Ta_u/S_u is the same as Ta_d/S_d in symmetric Ta_2CS_2 , while there is a distinct difference in asymmetric Ta_2CS_2 . This unbalanced charge distribution in asymmetric Ta_2CS_2 also results in the different bond lengths for $\text{Ta}_u\text{-C}$ and $\text{Ta}_d\text{-C}$ bonds, as contrasted with the equal bond lengths in symmetric Ta_2CS_2 (Table I), which is consistent with the interlayer sliding model in 2D ferroelectric materials [58].

To study the effect of charge redistribution on atom vibrations, we calculate the normalized traces of 2ND IFCs defined as [59]

$$|\text{Tr}(2\text{ND IFCs})| = \left| \frac{\sum_{\alpha} \Phi_{0,i}^{\alpha,\alpha}}{\sum_{\alpha} \Phi_{0,0}^{\alpha,\alpha}} \right|, \quad (7)$$

where $\Phi_{0,i}^{\alpha,\alpha}$ represents the 2ND IFCs in the α direction between the origin atom (u_0^α) and the i th neighboring atom (u_i^α). When $i = 0$, it represents the self-interaction 2ND IFCs, and the distance is defined as $d = |\mathbf{r}_i^0 - \mathbf{r}_0^0|$. The trace of 2ND IFCs quantifies the bonding stiffness and allows us to compare the interatomic interaction ranges in different structures and different bonding stiffness by normalizing the trace of 2ND IFCs.

The normalized traces of 2ND IFCs for Ta atoms vs the interaction distance are shown in Fig. 7. Corresponding to

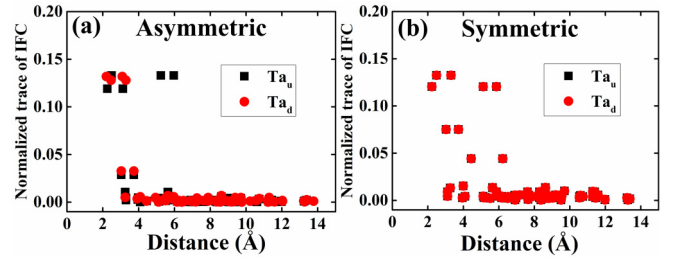


FIG. 7. Normalized traces of harmonic (2ND) interatomic force constants (IFCs) for Ta atoms in (a) asymmetric Ta_2CS_2 and (b) symmetric Ta_2CS_2 .

their crystal symmetry, the normalized trace of 2ND IFCs of Ta atoms in symmetric Ta_2CS_2 is the same, while the normalized trace of 2ND IFCs of Ta atoms in asymmetric Ta_2CS_2 is different. Surprisingly, the nonnegligible 2ND IFCs of Ta atoms can exist at a distance as long as 9 Å in symmetric Ta_2CS_2 . In contrast, the convergence radius of 2ND IFCs of Ta atoms in asymmetric Ta_2CS_2 is ~ 6 Å. This result suggests that the inversion symmetry breaking and the redistribution of charge in asymmetric Ta_2CS_2 cause the interatomic forces to converge at a shorter distance, so asymmetric Ta_2CS_2 has a stronger stability and harmonicity. In other words, the inversion symmetry breaking and the dipole in asymmetric Ta_2CS_2 make the system more stable and lead to the enhancement of lattice thermal conductivity compared with the symmetric case. Although the inversion symmetry of symmetric Ta_2CS_2 limits the phonon scattering, this factor does not play a dominant role due to the high-anharmonic scattering rates.

The above discussion reveals that the charge redistribution in real space is the physical origin for the change of the interatomic interactions, which further leads to the variation of harmonic/anharmonic properties. One notable example is the softening of the TO branch in symmetric Ta_2CS_2 , which indicates a lower stability [60,61]. The softened TO branch in ferroelectric materials is a particular normal mode of the crystal lattice, which exhibits a redshift in its characteristic frequency as the nonpolar-polar transition is approached. As shown in Fig. 2(c), the TO branch of symmetric Ta_2CS_2 is softened throughout the Brillouin zone and becomes more dispersive, especially around the K point [see the blue circle region in Fig. 2(c)], which represents the lower stability and stronger anharmonicity in symmetric Ta_2CS_2 .

Another interesting feature is the emergence of local regions with high scattering rates in Fig. 6, especially for symmetric Ta_2CS_2 ~ 3.5 THz (shadowed region in Fig. 6). This phenomenon is related to the LA-TO hybridization in the phonon dispersion of symmetric Ta_2CS_2 , which is indicated by the dashed circle region in the inset of Fig. 2(b). Previous works found the anticrossing phenomenon can reduce thermal

TABLE I. The charge transfer and atomic bond lengths for symmetric and asymmetric Ta_2CS_2 .

Type	Ta_u (e ⁻)	Ta_d (e ⁻)	C (e ⁻)	S_u (e ⁻)	S_d (e ⁻)	$\text{Ta}_u\text{-C}$ bond length (Å)	$\text{Ta}_d\text{-C}$ bond length (Å)
Symmetric	+1.80	+1.80	-1.92	-0.84	-0.84	2.225	2.225
Asymmetric	+1.66	+1.86	-1.90	-0.79	-0.83	2.252	2.194

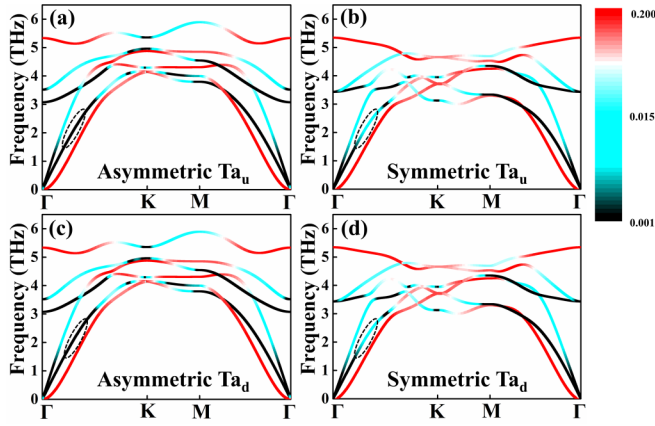


FIG. 8. Phonon band structures for the Z direction vibrations of the Ta_u/Ta_d atom in (a) and (c) asymmetric Ta_2CS_2 and (b) and (d) symmetric Ta_2CS_2 . The color represents the proportion of vibrations in the Z direction of the Ta atoms.

conductivity by increasing the scattering matrix elements [62]. Although the anticrossing phenomenon also appears in asymmetric Ta_2CS_2 , the negligible gap indicates a relatively weak hybridization between the LA and TO branches, corresponding to a lower peak in the same shadowed region in Fig. 6. Therefore, the different LA-TO coupling strength leads to the significantly different anharmonic scattering rates in this local region, which further enlarges the contrast in the anharmonic properties between symmetric and asymmetric Ta_2CS_2 .

To examine the degree of mode hybridization in the entire Brillouin zone, we finally calculate for each phonon mode the projection to the Z direction as [33]

$$F(Z, \mathbf{k}, i, \lambda) = |e_{\mathbf{k},\lambda}(i, Z)|^2, \quad (8)$$

where i is the atom index for the Ta atom, and $e_{\mathbf{k},\lambda}(i, Z)$ is the eigenvector of the atom i along the Z direction for phonon mode (\mathbf{k}, λ) . Figure 8 shows the weighted phonon dispersion, in which the color represents the value of projection function $F(Z, \mathbf{k}, i, \lambda)$. Obviously, the XY-Z hybridization (colored region) not only appears at the position of the LA-TO anticrossing but also exists in a wide range of other branches for both symmetric and asymmetric Ta_2CS_2 , due to the nonorthogonality of Ta-S bonds. This XY-Z hybridization phenomenon has also been reported in other 2D materials such as functionalized graphene and MoS_2 [33,63]. Moreover, the low-frequency TA phonons (dashed region $\sim 2\text{--}3$ THz in Fig. 8) in the asymmetric Ta_2CS_2 are purely in in-plane mode, while the same region in symmetric Ta_2CS_2 exhibits an obvious XY-Z hybridization. This result suggests that the inversion symmetry breaking leads to a weaker coupling between the in-plane and out-of-plane phonons, which is consistent with the weaker lattice anharmonicity observed in the lattice vibration (Fig. 5) and phonon scattering rate (Fig. 6).

Finally, we briefly discuss the experimental prospects of symmetric and asymmetric Ta_2CS_2 structures. There are literature works on the synthesis and applications of functionalized MXenes, especially for the symmetric phase of functionalized MXenes, which have demonstrated their stability and experimental availability [64–66]. Although the asymmetric phase of functionalized MXenes has not been prepared experimentally so far, many theoretical works have predicted this asymmetric phase and verified its stability [38,67,68]. Moreover, the tunable ferroelectricity in MXenes by surface functionalization has also been demonstrated in experiment [69]. Furthermore, compared with symmetric Ta_2CS_2 , the asymmetric Ta_2CS_2 structure has a lower energy according to our calculation, which suggests that the experimental synthesis of the asymmetric phase is feasible.

IV. CONCLUSIONS

We have investigated the thermal transport properties of two kinds of sulfur-functionalized Ta_2C with different symmetries by using the phonon Boltzmann transport theory combined with first-principles calculations. In sharp contrast with the mirror symmetry rule in graphene that promotes thermal transport, the thermal conductivity of asymmetric Ta_2CS_2 is much higher than that of symmetric Ta_2CS_2 . The variations of atomic position and symmetry have a strong impact on the anharmonic properties, which is reflected by the softened TO branch and the larger amplitude of atomic vibrations in symmetric Ta_2CS_2 compared with the asymmetric counterpart. The inversion symmetry breaking in Ta_2CS_2 reduces the phonon anharmonic scattering strength by one order of magnitude and weakens the XY-Z hybridization, which ultimately gives rise to a higher thermal conductivity in asymmetric Ta_2CS_2 . By analyzing the Bader charge, bond lengths, and the trace of 2ND IFCs, we confirm that variation of interlayer spacing between Ta-C redistributes the charge and induces the out-of-plane polarization. The rearrangement of charge in Ta atoms is the physical origin for the observed difference in anharmonic properties between symmetric and asymmetric Ta_2CS_2 . The huge difference in thermal conductivity between nonpolar-polar Ta_2CS_2 might have a potential application as a thermal switch. In this paper, we provide insight into role of symmetry on the thermal transport in 2D functionalized MXenes.

ACKNOWLEDGMENTS

This project is supported in part by grants from the National Natural Science Foundation of China (Grants No. 12075168 and No. 11890703), the Science and Technology Commission of Shanghai Municipality (Grants No. 19ZR1478600 and No. 21JC1405600), and the Fundamental Research Funds for the Central Universities (Grant No. 22120220060).

[1] G. J. Snyder and E. S. Toberer, *Nat. Mater.* **7**, 105 (2008).

[2] M. Rull-Bravo, A. Moure, J. F. Fernandez, and M. Martin-Gonzalez, *RSC Adv.* **5**, 41653 (2015).

- [3] P. Sundarraj, D. Maity, S. S. Roy, and R. A. Taylor, *RSC Adv.* **4**, 46860 (2014).
- [4] G. Tan, L. D. Zhao, and M. G. Kanatzidis, *Chem. Rev.* **116**, 12123 (2016).
- [5] Y. Ouyang, Z. Zhang, D. Li, J. Chen, and G. Zhang, *Ann. Phys. (Berlin)* **531**, 1800437 (2019).
- [6] C. Gayner and K. K. Kar, *Prog. Mater. Sci.* **83**, 330 (2016).
- [7] G. Zhang and Y. W. Zhang, *J. Mater. Chem. C* **5**, 7684 (2017).
- [8] L. Shi, J. Chen, G. Zhang, and B. Li, *Phys. Lett. A* **376**, 978 (2012).
- [9] J. R. Sootsman, D. Y. Chung, and M. G. Kanatzidis, *Angew. Chem.-Int. Edit* **48**, 8616 (2009).
- [10] Z. Zhang, Y. Ouyang, Y. Cheng, J. Chen, N. Li, and G. Zhang, *Phys. Rep.* **860**, 1 (2020).
- [11] K. F. Hsu, S. Loo, F. Guo, W. Chen, J. S. Dyck, C. Uher, T. Hogan, E. K. Polychroniadis, and M. G. Kanatzidis, *Science* **303**, 818 (2004).
- [12] J. L. Mi, T. J. Zhu, X. B. Zhao, and J. Ma, *J. Appl. Phys.* **101**, 054314 (2007).
- [13] M. S. Toprak, C. Stiewe, D. Platzek, S. Williams, L. Bertini, E. C. Muller, C. Gatti, Y. Zhang, M. Rowe, and M. Muhammed, *Adv. Funct. Mater.* **14**, 1189 (2004).
- [14] J. F. Li, W. S. Liu, L. D. Zhao, and M. Zhou, *NPG Asia Mater.* **2**, 152 (2010).
- [15] W. Ren, Y. Ouyang, P. Jiang, C. Yu, J. He, and J. Chen, *Nano Lett.* **21**, 2634 (2021).
- [16] M. Christensen, A. B. Abrahamsen, N. B. Christensen, F. Juranyi, N. H. Andersen, K. Lefmann, J. Andreasson, C. R. Bahl, and B. B. Iversen, *Nat. Mater.* **7**, 811 (2008).
- [17] T. Tadano, Y. Gohda, and S. Tsuneyuki, *Phys. Rev. Lett.* **114**, 095501 (2015).
- [18] Z. Zhang, S. Hu, T. Nakayama, J. Chen, and B. Li, *Carbon* **139**, 289 (2018).
- [19] T. Ouyang, Q. Liu, M. Chen, C. Tang, J. Li, C. Zhang, C. He, H. Bao, J. Zhong, and M. Hu, *ES Energy Environ.* **3**, 88 (2019).
- [20] S. Lu, Y. Ouyang, C. Yu, P. Jiang, J. He, and J. Chen, *J. Appl. Phys.* **129**, 225106 (2021).
- [21] K. Biswas, J. He, I. D. Blum, C. I. Wu, T. P. Hogan, D. N. Seidman, V. P. Dravid, and M. G. Kanatzidis, *Nature (London)* **489**, 414 (2012).
- [22] R. M. Murphy, É. D. Murray, S. Fahy, and I. Savić, *Phys. Rev. B* **95**, 144302 (2017).
- [23] S. Y. Yue, H. T. Chorsi, M. Goyal, T. Schumann, R. Q. Yang, T. S. Xu, B. W. Deng, S. Stemmer, J. A. Schuller, and B. L. Liao, *Phys. Rev. Research* **1**, 033101 (2019).
- [24] J. Chen, G. Zhang, and B. Li, *Appl. Phys. Lett.* **95**, 073117 (2009).
- [25] Y. Li, Y. P. Yi, V. Coropceanu, and J. L. Bredas, *Phys. Rev. B* **85**, 245201 (2012).
- [26] J. L. Manes, *Phys. Rev. B* **76**, 045430 (2007).
- [27] Y. Machida, S. Nakatsuji, S. Onoda, T. Tayama, and T. Sakakibara, *Nature (London)* **463**, 210 (2010).
- [28] V. P. Gusynin, V. A. Miransky, and I. A. Shovkovy, *Phys. Rev. D* **52**, 4718 (1995).
- [29] Y. Gorodetski, N. Shitrit, I. Bretner, V. Kleiner, and E. Hasman, *Nano Lett.* **9**, 3016 (2009).
- [30] W. Shen, C. Hu, J. Tao, J. Liu, S. Fan, Y. Wei, C. An, J. Chen, S. Wu, Y. Li *et al.*, *Nanoscale* **10**, 8329 (2018).
- [31] L. Lindsay, D. A. Broido, and N. Mingo, *Phys. Rev. B* **82**, 115427 (2010).
- [32] L. F. Huang and Z. Zeng, *J. Phys. Chem. C* **119**, 18779 (2015).
- [33] L. F. Huang, P. L. Gong, and Z. Zeng, *Phys. Rev. B* **90**, 045409 (2014).
- [34] M. Naguib, V. N. Mochalin, M. W. Barsoum, and Y. Gogotsi, *Adv. Mater.* **26**, 992 (2014).
- [35] J. L. Hart, K. Hantanasirisakul, A. C. Lang, B. Anasori, D. Pinto, Y. Pivak, J. T. van Omme, S. J. May, Y. Gogotsi, and M. L. Taheri, *Nat. Commun.* **10**, 522 (2019).
- [36] J. Walter, W. Boonchuduang, and S. Hara, *J. Alloy. Compd.* **305**, 259 (2000).
- [37] K. Sakamaki, H. Wada, H. Nozaki, Y. Onuki, and M. Kawai, *J. Alloy. Compd.* **339**, 283 (2002).
- [38] L. Zhang, C. Tang, C. Zhang, and A. Du, *Nanoscale* **12**, 21291 (2020).
- [39] S. Sarikurt, D. Cakir, M. Keceli, and C. Sevik, *Nanoscale* **10**, 8859 (2018).
- [40] G. Kresse, J. Furthmuller, and J. Hafner, *Phys. Rev. B* **50**, 13181 (1994).
- [41] G. Kresse and J. Hafner, *Phys. Rev. B* **49**, 14251 (1994).
- [42] J. P. Perdew, K. Burke, and M. Ernzerhof, *Phys. Rev. Lett.* **77**, 3865 (1996).
- [43] H. J. Monkhorst and J. D. Pack, *Phys. Rev. B* **13**, 5188 (1976).
- [44] J. Neugebauer and M. Scheffler, *Phys. Rev. B* **46**, 16067 (1992).
- [45] A. Togo and I. Tanaka, *Scripta Mater.* **108**, 1 (2015).
- [46] W. Li, J. Carrete, N. A. Katcho, and N. Mingo, *Comput. Phys. Commun.* **185**, 1747 (2014).
- [47] J. He, Y. Ouyang, C. Yu, P. Jiang, W. Ren, and J. Chen, *Chin. Phys. B* **29**, 126503 (2020).
- [48] Y. Ouyang, Z. Zhang, C. Yu, J. He, G. Yan, and J. Chen, *Chin. Phys. Lett.* **37**, 126301 (2020).
- [49] Y. Ouyang, C. Yu, J. He, P. Jiang, W. Ren, and J. Chen, *Phys. Rev. B* **105**, 115202 (2022).
- [50] D. A. Broido, A. Ward, and N. Mingo, *Phys. Rev. B* **72**, 014308 (2005).
- [51] S. Baroni, S. de Gironcoli, A. Dal Corso, and P. Giannozzi, *Rev. Mod. Phys.* **73**, 515 (2001).
- [52] Y. Wang, J. J. Wang, W. Y. Wang, Z. G. Mei, S. L. Shang, L. Q. Chen, and Z. K. Liu, *J. Phys.: Condens. Matter* **22**, 202201 (2010).
- [53] L. Zhu, W. Li, and F. Ding, *Nanoscale* **11**, 4248 (2019).
- [54] R. Yang, S. Yue, Y. Quan, and B. Liao, *Phys. Rev. B* **103**, 184302 (2021).
- [55] R. Gupta, B. Dongre, C. Bera, and J. Carrete, *J. Phys. Chem. C* **124**, 17476 (2020).
- [56] G. Henkelman, A. Arnaldsson, and H. Jónsson, *Comput. Mater. Sci.* **36**, 354 (2006).
- [57] E. Sanville, S. D. Kenny, R. Smith, and G. Henkelman, *J. Comput. Chem.* **28**, 899 (2007).
- [58] W. Ding, J. Zhu, Z. Wang, Y. Gao, D. Xiao, Y. Gu, Z. Zhang, and W. Zhu, *Nat. Commun.* **8**, 14956 (2017).
- [59] S. Lee, K. Esfarjani, T. Luo, J. Zhou, Z. Tian, and G. Chen, *Nat. Commun.* **5**, 3525 (2014).
- [60] R. Blinc, *Ferroelectrics* **74**, 301 (1987).
- [61] C. W. Li, J. Hong, A. F. May, D. Bansal, S. Chi, T. Hong, G. Ehlers, and O. Delaire, *Nat. Phys.* **11**, 1063 (2015).
- [62] W. Li, J. Carrete, G. K. H. Madsen, and N. Mingo, *Phys. Rev. B* **93**, 205203 (2016).
- [63] L. F. Huang, T. F. Cao, P. L. Gong, and Z. Zeng, *Solid State Commun.* **190**, 5 (2014).

- [64] A. Ostadhossein, J. Guo, F. Simeski, and M. Ihme, [Comm. Chem.](#) **2**, 95 (2019).
- [65] M. Mozafari and M. Soroush, [Mater. Adv.](#) **2**, 7277 (2021).
- [66] R. Ibragimova, P. Erhart, P. Rinke, and H. P. Komsa, [J. Phys. Chem. Lett.](#) **12**, 2377 (2021).
- [67] Z. Wang, N. Ding, C. Gui, S.-S. Wang, M. An, and S. Dong, [Phys. Rev. Materials](#) **5**, 074408 (2021).
- [68] A. Chandrasekaran, A. Mishra, and A. K. Singh, [Nano Lett.](#) **17**, 3290 (2017).
- [69] J. Kim, M. Jang, G. Jeong, S. Yu, J. Park, Y. Lee, S. Cho, J. Yeom, Y. Lee, A. Choe *et al.*, [Nano Energy](#) **89**, 106409 (2021).